

1 **Different effects of anthropogenic emissions and aging processes on the**  
2 **mixing state of soot particles in the nucleation and accumulation**  
3 **modes**

4

5 Yuying Wang<sup>1,2</sup>, Rong Hu<sup>1,2</sup>, Qiuyan Wang<sup>1</sup>, Zhanqing Li<sup>3</sup>, Maureen Cribb<sup>3</sup>, Yele Sun<sup>4</sup>, Xiaorui  
6 Song<sup>1</sup>, Yi Shang<sup>1</sup>, Yixuan Wu<sup>1</sup>, Xin Huang<sup>1</sup>, Yuxiang Wang<sup>1</sup>

7

8 <sup>1</sup> Key Laboratory for Aerosol-Cloud-Precipitation of China Meteorological Administration, School  
9 of Atmospheric Physics, Nanjing University of Information Science & Technology, Nanjing  
10 210044, China

11 <sup>2</sup> State Key Laboratory of Remote Sensing Science, College of Global Change and Earth System  
12 Science, Beijing Normal University, Beijing 100875, China

13 <sup>3</sup> Earth System Science Interdisciplinary Center, Department of Atmospheric and Oceanic Science,  
14 University of Maryland, College Park, MD, USA

15 <sup>4</sup> State Key Laboratory of Atmospheric Boundary Layer Physics and Atmospheric Chemistry,  
16 Institute of Atmospheric Physics, Chinese Academy of Sciences, Beijing, 100029, China

17

18 Correspondence to: Yuying Wang (yuyingwang@nuist.edu.cn)

19 **Abstract.** In this study, the mixing state of size-resolved soot particles and their influencing factors  
20 were investigated based on a five-month aerosol volatility measurement at a suburban site (Xingtai,  
21 XT) in the central North China Plain (NCP). The volatility and mixing state of soot-containing  
22 particles at XT were complex caused by multiple pollution sources and various aging processes.  
23 The results suggest that anthropogenic emissions can weaken the mean volatility of soot-containing  
24 particles and enhance their degree of external mixing. There were fewer externally mixed soot  
25 particles in warm months (June, July, and August) than in cold months (May, September, and  
26 October). Monthly variations in the mean coating depth ( $D_{c,mean}$ ) of volatile matter on soot particles  
27 showed that the coating effect was stronger in warm months than in cold months, even though  
28 aerosol pollution was heavier in cold months. Moreover, the volatility was stronger, and the degree  
29 of internal mixing was higher in nucleation-mode soot-containing particles than in accumulation-  
30 mode soot-containing particles. Relationships between  $D_{c,mean}$  and possible influencing factors  
31 [temperature ( $T$ ), relative humidity (RH), and particulate matter with diameters ranging from 10 to  
32 400 nm] further suggest that high ambient  $T$  and RH in a polluted environment could promote the  
33 coating growth of accumulation-mode soot particles. However, high ambient  $T$  but low RH in a  
34 clean environment were beneficial to the coating growth of nucleation-mode soot particles. Our  
35 results highlight the diverse impact of anthropogenic emissions and aging processes on the mixing  
36 state of soot particles in different modes, which should be considered separately in models to  
37 improve the simulation accuracy of aerosol absorption.

## 39 1. Introduction

40 Aerosols are mixed liquid and solid particles suspended in the atmosphere. Some aerosols are  
41 directly produced from natural or anthropogenic sources (i.e., primary aerosols), and the rest are  
42 indirectly transformed from gas precursors through atmospheric chemical reactions (i.e., secondary  
43 aerosols). The newly formed particles can grow or shrink through various aging processes (e.g.,  
44 condensation, coagulation, volatilization, chemical reactions). Aerosol physicochemical properties  
45 (number concentration, shape, mixing state, optical properties, among others) are thus highly  
46 variable. This is one of the reasons why aerosols are highly uncertain in climate change assessments  
47 (Bond et al., 2013; Seinfeld et al., 2016; Bellouin et al., 2020; Christensen et al., 2021). Although  
48 great efforts have been made to understand aerosol optical properties, the uncertainty of radiative  
49 forcing caused by aerosols is still two to three times that of greenhouse gases (IPCC, 2021).

50 Aerosols can affect the earth-atmosphere radiation balance by scattering or absorbing shortwave  
51 and longwave radiation, which is called the aerosol direct climate effect or aerosol-radiation  
52 interactions. Many factors, such as aerosol chemical composition, mixing state, and ambient relative  
53 humidity (RH), have complex impacts on aerosol-radiation interactions (e.g., Twohy et al., 2009;

54 Kuniyal and Guleria, 2019; Ren et al., 2021). According to the sixth IPCC report, the total direct  
55 radiative forcing caused by anthropogenic aerosols is generally negative. However, light-absorbing  
56 carbonaceous particles (LAC) have a warming effect on climate (Ramana et al., 2010; Gustafsson  
57 and Ramanathan, 2016), which can partly offset the cooling effect caused by scattering aerosols,  
58 such as sulfate. Black carbon (BC) is the most important LAC compound, mostly emitted as soot  
59 from anthropogenic sources (incomplete fossil fuel combustion and biomass burning) (Novakov et  
60 al., 2003). Some experiments have suggested that BC in urban polluted environments can play an  
61 important role in pollution formation and development. The internal mixing of BC with secondly  
62 formed matter could also greatly enhance light absorption (Peng et al., 2016; Zhou et al., 2017).

63 The online measurement instruments quantifying the mixing state of BC-containing particles are  
64 limited. Based on the measurement of single-particle soot photometer (SP2), Wu et al. (2017)  
65 indicated that the mass of refractory black carbon (*r*BC) had an approximately lognormal  
66 distribution as a function of the volume-equivalent diameter (VED) in Beijing. Yu et al. (2020)  
67 suggested that the mixing state of *r*BC particles was related to air pollution levels and air mass  
68 sources. Zhang et al. (2021) further indicated that meteorological conditions had a large impact on  
69 the mixing state of *r*BC particles. Moreover, the Aerodyne soot particle aerosol mass spectrometer  
70 (SP-AMS) can also be used to study the mixing state of *r*BC. For example, J. Wang et al. (2019)  
71 found that the formation of secondary aerosols through photochemical and aqueous chemical  
72 reactions was responsible to the coating of *r*BC based on the measurement of SP-AMS in winter  
73 Beijing. However, the lower observation limit of particle size by SP2 and SP-AMS is larger than  
74 ~70 nm. Therefore, they cannot quantify the mixing state of BC-containing particles in the small  
75 nucleation mode. Modern gasoline direct injection (GDI) vehicles can emit plentiful ultrafine BC-  
76 containing (soot) particles in the ambient (La Rocca et al., 2015; Hu et al., 2021). The tiny soot  
77 particles embedded in other material (such as sulfate) play a significant role in particle growth (Li  
78 et al., 2011). Investigating the mixing state of BC-containing particles and their factors in different  
79 modes are needed.

80 Aerosol volatility refers to the shrinking extent of particles at a certain temperature. The mixing  
81 state of soot particles or tarballs is closely related to aerosol volatility at high temperatures (Philippin  
82 et al., 2004; Wehner et al., 2009; Adachi et al., 2018, 2019). Most primary soot particles from  
83 anthropogenic sources are refractory, hydrophobic, and externally mixed. In a polluted environment,  
84 primary soot particles are easily transformed to internally mixed particles through certain coating  
85 processes in the atmosphere (Cheng et al., 2012; Peng et al., 2016; F. Zhang et al., 2020). However,  
86 coating matter is generally non-refractory because most of the matter consists of secondary chemical  
87 species, such as organics, sulfate, and nitrate (Philippin et al., 2004; Hong et al., 2017). This is why  
88 aerosol volatility can characterize the mixing state of soot particles in polluted environments

89 (Wehner et al., 2009; Hossain et al., 2012; S. Zhang et al., 2016). A volatility tandem differential  
90 mobility analyzer (VTDMA) is usually used to quantify aerosol volatility by measuring the change  
91 in particle size at a set temperature. Aerosol volatility measured by a VTDMA at a high temperature  
92 (> 280°C) can be used to study the mixing state of soot particles (Philippin et al., 2004; Wehner et  
93 al., 2009; Y. Zhang et al., 2016; Wang et al., 2017). Meanwhile, VTDMA measurements are based  
94 on the aerosol number concentration, which is always high in the nucleation mode in the ~~actual~~  
95 ~~atmosphereambient~~. Therefore, VTDMA can quantify the mixing state of nucleation-mode soot  
96 particles.

97 Over the past years, several studies have reported the volatility and mixing state of ~~soot-~~  
98 ~~containing~~ particles based on VTDMA measurements in the North China Plain (NCP). For example,  
99 Wehner et al. (2009) found that the mixing state of soot particles in Beijing and its surrounding  
100 region varied, especially between new particle formation days and heavily polluted days. Using the  
101 same VTDMA and aerosol optical data, Cheng et al. (2009) conducted an aerosol optical closure  
102 study, finding that soot aging was rapid at the Yufa site south of Beijing. The coating on soot particles  
103 can enhance aerosol absorption and scattering coefficients by a factor of 8 to 10 within several hours  
104 due to secondary processing during the daytime, which is the combined effect of the increased  
105 thickness of the coating shell and the transition of soot from an externally mixed state to a coated  
106 state. Cheng et al. (2012) further indicated that aging and emissions were two competing factors in  
107 the mixing state of soot particles. Based on VTDMA measurement data collected in 2015, Wang et  
108 al. (2017) indicated that strict emission control measures implemented in Beijing and surrounding  
109 areas could enhance the volatility of soot-containing particles and their degrees of external mixing.  
110 At another regional site (Xianghe) in the northern part of the NCP, S. Zhang et al. (2016) found that  
111 the mixing state of ambient particles was complex with different volatilities. Furthermore, Y. Zhang  
112 et al. (2016) suggested that the average shell-to-core ratio and absorption enhancement ( $E_{ab}$ ) of  
113 ambient BC was 2.1–2.7 and 1.6–1.9, respectively.

114 These studies imply that anthropogenic emissions play an important role in the volatility and  
115 mixing state of soot-containing particles and that the coating on soot particles can greatly enhance  
116 aerosol absorption. However, these studies were based on data collected during short-term  
117 observational periods in the northern part of the NCP and they did not distinguish the factors  
118 influencing the mixing state of nucleation- and accumulation-mode soot particles. Recent studies  
119 (Y. Wang et al., 2018, 2019, 2021) have shown that anthropogenic sources and aerosol aging  
120 processes are various in the north and central-south NCP, leading to diverse aerosol physiochemical  
121 properties between these regions in different seasons. More research about the mixing state of soot  
122 particles in the central-south NCP is needed to improve the accuracy of modeled aerosol optical  
123 properties.

124 This study investigates for the first time the volatility and mixing state of nucleation- and  
125 accumulation-mode soot-containing particles in the warm and cold seasons based on one  
126 comprehensive field campaign that took place in the central NCP, lasting five months. Exploring  
127 factors influencing the volatility and mixing state of soot-containing particles in this study will  
128 improve the accuracy of modeled aerosol optical properties in the central NCP. This paper is  
129 organized as follows. Section 2 introduces the sampling site, instruments, and data analysis. Section  
130 3 presents the results and discussion, including meteorological conditions, aerosol pollution levels,  
131 changes in volatility and mixing state of soot-containing particles, and their influencing factors.  
132 Section 4 gives conclusions and summarizes the study.

133

## 134 2. Sampling site, instruments, and data analysis

### 135 2.1 Sampling site

136 Data used in this study were collected at the National Meteorological Basic Station (37°11'N,  
137 114°22'E, 180 m above sea level) in Xingtai (XT), China, equipped with a variety of meteorological  
138 observation instruments. The measured meteorological variables including ambient temperature,  
139 relative humidity (RH), wind direction and speed ~~were~~ used in this study. Y. Wang et al. (2018)  
140 reported that this site ~~is~~-was located in a polluted area of the central-south NCP, influenced by  
141 multiple anthropogenic sources, such as industrial coal firing, fossil-fuel burning, agricultural  
142 activities, and household emissions. The long-distance transport of pollutants also influences the air  
143 quality at XT. Previous studies have suggested that air pollution at XT represents well regional  
144 pollution characteristics in the central NCP, east of the Taihang Mountains (Y. Zhang et al., 2018;  
145 Y. Wang et al., 2018). A comprehensive field campaign named the Atmosphere-Aerosol-Boundary  
146 layer-Cloud (A<sup>2</sup>BC) Interaction Joint Experiment was carried out at XT from May to October of  
147 2016. Y. Wang et al. (2018) and Li et al. (2019) provide details about the XT site and the A<sup>2</sup>BC  
148 campaign. Here, over five months of aerosol observational data, including particle number size  
149 distribution (PNSD), aerosol volatility, and BC mass concentration, were used to analyze the  
150 volatility and mixing state of soot particles and their influencing factors.

151

### 152 2.2 Instruments

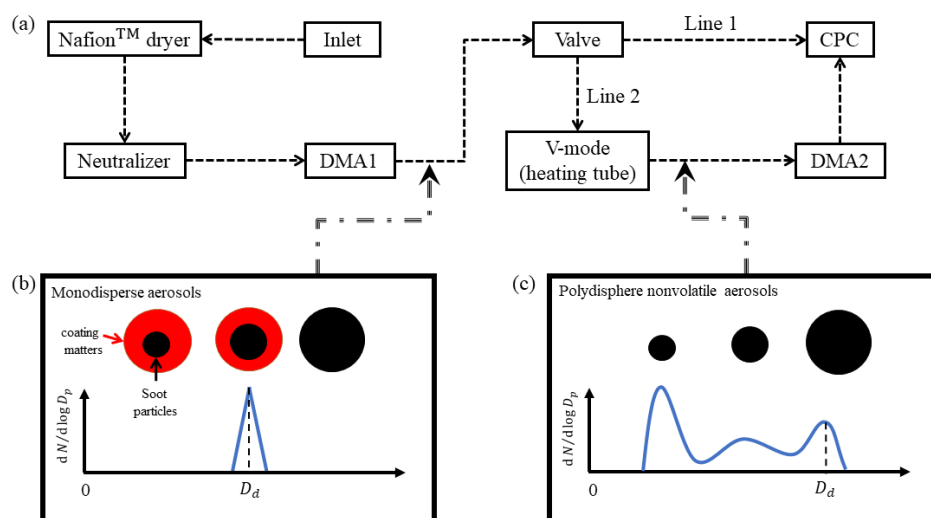
#### 153 2.2.1 Measuring PNSD and aerosol volatility

154 The tandem differential mobility analyzer (TDMA) system is widely used to measure the change  
155 in particle size under special conditions, e.g., high humidity, high temperature, and chamber  
156 chemical reactions (Swietlicki et al., 2008). In this campaign, the VTDMA system was used to  
157 measure aerosol volatility at 300°C. The inlet air sample was first dried by a Nafion™ dryer to low  
158 RH (< 30%), then neutralized by a soft X-ray neutralizer (model 3088, TSI Inc.; Fig. 1a). Afterwards,

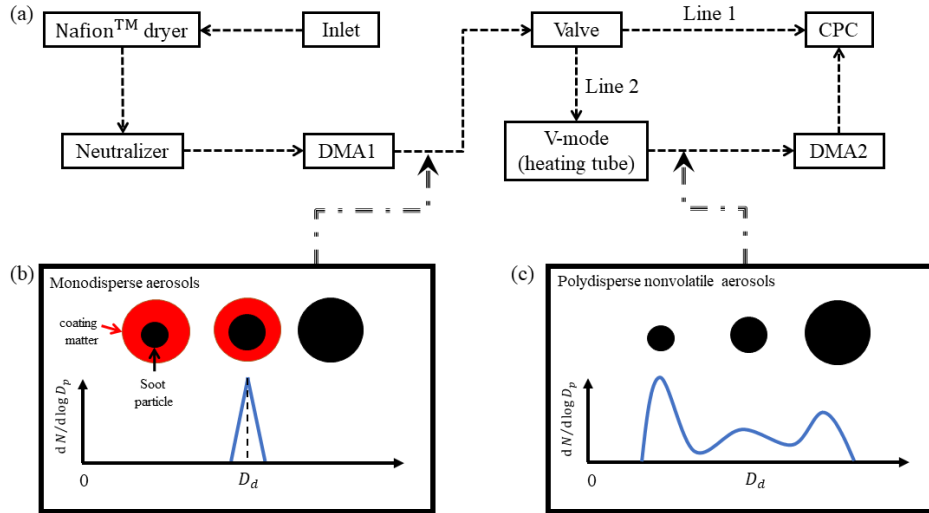
159 quasi-monodisperse aerosols (Fig. 1b) with a certain dried diameter ( $D_d$ ) were split by the first  
 160 differential mobility analyzer (DMA1). In this campaign,  $D_d$  was set to 40, 80, 110, 150, 200, and  
 161 300 nm. An automated valve located after the DMA1 had two outlet lines. Line 1 directly accessed  
 162 the water-based condensation particle counter (WCPC, model 3787, TSI Inc.), measuring the  
 163 number concentration of particles ranging from 10 to 400 nm. Line 2 accessed a heating tube,  
 164 vaporizing volatile materials at a controlled high temperature (300°C in this study). The ratio of  
 165 particle size after volatilization [ $D_p(T)$ ] to  $D_d$  is defined as the aerosol shrink factor (i.e.,  $SF = D_p(T)$   
 166 /  $D_d$ ). After heating, residual aerosols were generally polydisperse nonvolatile particles (Fig. 1c).  
 167 The second DMA (DMA2) and WCPC were used to measure the number size distribution of  
 168 nonvolatile particles, measuring the distribution function of  $SF$  ( $SF$ -MDF). Finally, the probability  
 169 density function of  $SF$  ( $SF$ -PDF) was retrieved using the TDMAfit algorithm (Stolzenburg and  
 170 McMurry, 1988; Stolzenburg and McMurry, 2008).

171 In this study, we assume that the shape of all particles follows the core-shell model (nonvolatile  
 172 core and volatile shell; Fig. 1b). Residual particles after volatilization have different-sized  
 173 nonvolatile cores (Fig. 1c). Previous studies have suggested that residual particles at 300°C mainly  
 174 consist of soot (Philippin et al., 2004; Wehner et al., 2009). Aerosol volatility measured by the  
 175 VTDMA in this study can thus reflect the degree of mixing state of soot particles. \_

176  
 177



178



179  
180 **Figure 1.** Schematic diagram of the volatility tandem differential mobility analyzer used in this  
181 study.

182 —  
183 2.2.2 Measuring BC

184 In this campaign, a seven-wavelength aethalometer (model AE-33, Magee Scientific Corp.) was  
185 used to measure the mass concentration of BC ( $M_{BC}$ ). After calibration, the sampling flow rate of  
186 the AE-33 was  $5.0 \text{ L min}^{-1}$ . A cyclone with particulate matter (diameters =  $2.5 \mu\text{m}$ , or  $\text{PM}_{2.5}$ ) was  
187 used in the sample inlet. Aerosol particles were collected on filter tape through a spot, and the  
188 instantaneous concentration of optically absorbing aerosols was retrieved from the rate of change  
189 of the attenuation of light transmitted through the filter. The wavelength channels of the AE-33 were  
190 370, 470, 525, 590, 660, 880, and 940 nm. According to the manufacturer's instructions, the  $M_{BC}$   
191 is calculated from the change in optical attenuation at channel 6 (i.e., 880 nm) in the selected time  
192 interval using the mass absorption cross section (MAC) of  $7.77 \text{ m}^2 \text{ g}^{-1}$ . The dependency of MAC on  
193 BC coating may introduce some uncertain in calculating MAC (Drinovec et al., 2015).

194  
195 2.2.3 VTDMA data analysis

196 The retrieved  $SF$ -PDF ( $c(D_d, SF)$ ) is normalized as  $\int c(D_d, SF) dSF = 1$ . The ensemble mean  
197 shrink factor ( $SF_{\text{mean}}$ ) is then calculated as

$$198 \quad SF_{\text{mean}}(D_d) = \int_0^{\infty} SF \cdot c(D_d, SF) dSF \quad (1)$$

199 Particles can be classified into several volatile groups according to different  $SF$  ranges (Y.  
200 Wang et al., 2017). The number fraction ( $NF$ ) for each volatile group with the  $SF$  boundary of  $[a, b]$   
201 is calculated as

$$202 \quad NF(D_d) = \int_a^b c(D_d, SF) dSF \quad (2)$$

203 Based on the core-shell assumption, the coating depth ( $D_c$ ) of soot particles is defined as the



204 depth of shell materials (i.e., shell depth). According to the definition of  $SF$ ,  $D_c$  for the particle  
 205 ( $D_d, SF$ ) can be calculated as

$$206 \quad D_c(D_d, SF) = \frac{D_d}{2}(1 - SF). \quad (3)$$

207 The ensemble mean  $D_c$  ( $D_{c,mean}$ ) using the normalized  $SF$ -PDF data is then calculated as

$$208 \quad D_{c,mean}(D_d) = \int_0^{\infty} D_c(D_d, SF) \cdot c(D_d, SF) dSF. \quad (4)$$

209

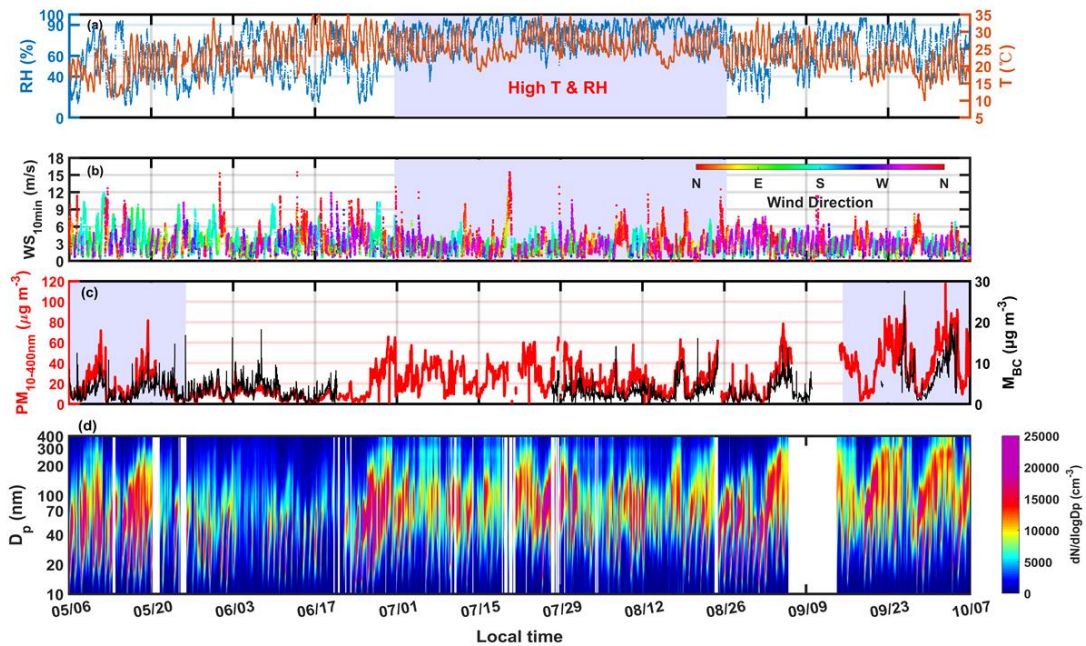
### 210 3. Results and discussion

#### 211 3.1 Meteorological conditions and aerosol pollution levels

212 Figure 1a-b shows the time series of ambient temperature ( $T$ ), RH, and wind direction and  
 213 speed (WD and WS, respectively) during the campaign. Monthly changes in  $T$  are clearly seen (Fig.  
 214 2a). Average  $T$ s in warm (June, July, and August) and cold (May, September, and October) months  
 215 were  $25.73 \pm 3.80$  and  $19.0 \pm 5.74^\circ\text{C}$ , respectively. The meteorological variables changed periodically  
 216 in cold months but not in warm months, which is caused by the cold fronts in cold months. Figure  
 217 2a also suggests that RH was higher in July and August than in other months.

218 Figure 2b shows that the wind changed significantly in different months at XT. Monthly wind  
 219 rose diagrams (Fig. S1) indicate that northwest winds prevailed in all months, caused by the special  
 220 terrain around XT (Y. Zhang et al., 2018). In July, weak southeast winds were also present,  
 221 beneficial to the accumulation of air pollutants due to the stable atmospheric environment. In August,  
 222 the other prevailing wind was from the north, which was beneficial for atmospheric diffusion.

223



224

225 **Figure 2.** Time series of (a) ambient relative humidity (RH; unit: %), and temperature ( $T$ ; unit:  $^\circ\text{C}$ ),



226 (b) wind direction (WD) and 10-minute-averaged wind speed (WS; unit:  $\text{m s}^{-1}$ ), (c) mass  
227 concentration of 10–400 nm particles ( $\text{PM}_{10-400}$ , in red; unit:  $\mu\text{g m}^{-3}$ ), assuming that the aerosol  
228 density is  $1.6 \text{ g cm}^{-3}$ , and mass concentration of black carbon ( $M_{\text{BC}}$ , in black; unit:  $\mu\text{g m}^{-3}$ ), and (d)  
229 particle number size distribution at the Xingtai site from 6 May 2016 to 6 October 2016.

230

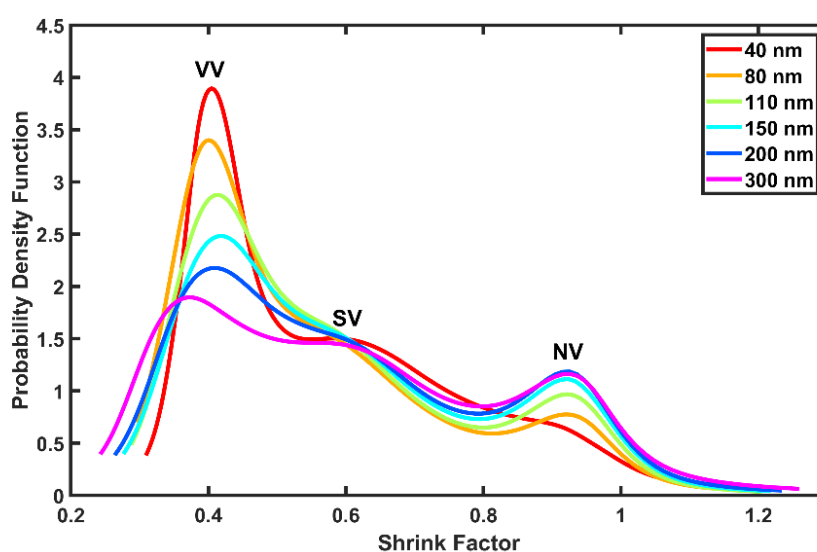
231 In this study, the total mass concentration of 10–400-nm particles ( $\text{PM}_{10-400}$ ) (Fig. 2c) was  
232 calculated using PNSD data (Fig. 2d), assuming that the aerosol density was  $1.6 \text{ g cm}^{-3}$  (Y. Wang  
233 et al., 2017). The average  $\text{PM}_{10-400}$  concentrations in warm and cold months were  $19.68 \pm 13.58$  and  
234  $29.79 \pm 21.37 \mu\text{g m}^{-3}$ , respectively, indicating much higher aerosol pollution in cold months than in  
235 warm months. In cold months,  $\text{PM}_{10-400}$  accumulated periodically as accumulation-mode ( $D_p > 100$   
236 nm) particles increased. This is closely related to cyclic changes in general atmospheric circulation,  
237 reflected by the cycle of winds (Fig. 2b). However,  $\text{PM}_{10-400}$  was lower in May than in September  
238 and October, likely due to the weaker particle growth in May. During warm months,  $\text{PM}_{10-400}$   
239 reached its lowest value in June with the lowest number concentration of accumulation-mode  
240 particles of all months (Fig. S2), suggesting that meteorological conditions in June were not  
241 conducive to particle growth. The high  $T$  and RH in July and August were beneficial to particle  
242 growth by promoting atmospheric photochemical and liquid chemical reactions (Z. Wu et al., 2018;  
243 Peng et al., 2021). Figure 2c suggests that  $\text{PM}_{10-400}$  was much higher in July and August than in June,  
244 although the mass concentrations of black carbon ( $M_{\text{BC}}$ ) in these months were considerable.  
245 However,  $\text{PM}_{10-400}$  was lower in August than in July, likely because of the better atmospheric  
246 diffusion conditions (more and stronger northerly winds) in August. Figure 2c also shows that  
247 changes in  $M_{\text{BC}}$  and  $\text{PM}_{10-400}$  were similar, suggesting the possible role of BC in the formation  
248 processes of aerosol pollution. Recently, F. Zhang et al. (2020) demonstrated that BC-catalyzed  
249 sulfate formation involving  $\text{NO}_2$  and  $\text{NH}_3$  plays an important role in the formation of haze events.

250

### 251 3.2 Monthly and diurnal variations in $SF$ -PDF

252 Figure 3 shows the size-resolved mean  $SF$ -PDFs at XT. In general,  $SF$ -PDFs had three peak  
253 modes, namely, at  $SF \approx 0.4$  [very volatile (VV) mode],  $0.6$  [slightly volatile (SV) mode], and  $0.9$   
254 [nonvolatile (NV) mode]. The trimodal distributions of  $SF$ -PDFs at XT in the central NCP differ  
255 from those at sites in the northern NCP (S. Zhang et al., 2016; Y. Wang et al., 2017), implying  
256 highly complex volatility and mixing state of soot particles at XT. Note that the  $SF$ -PDF of 40-nm  
257 particles has a quasi-unimodal distribution pattern, with low fractions of NV- and SV-mode  
258 particles. Previous studies have indicated that most NV-mode particles are externally mixed soot  
259 particles (Cheng et al., 2012; Cheung et al., 2016). This suggests that soot-containing particles in  
260 nucleation mode (represented by 40-nm particles) in this study had strong volatility and a high

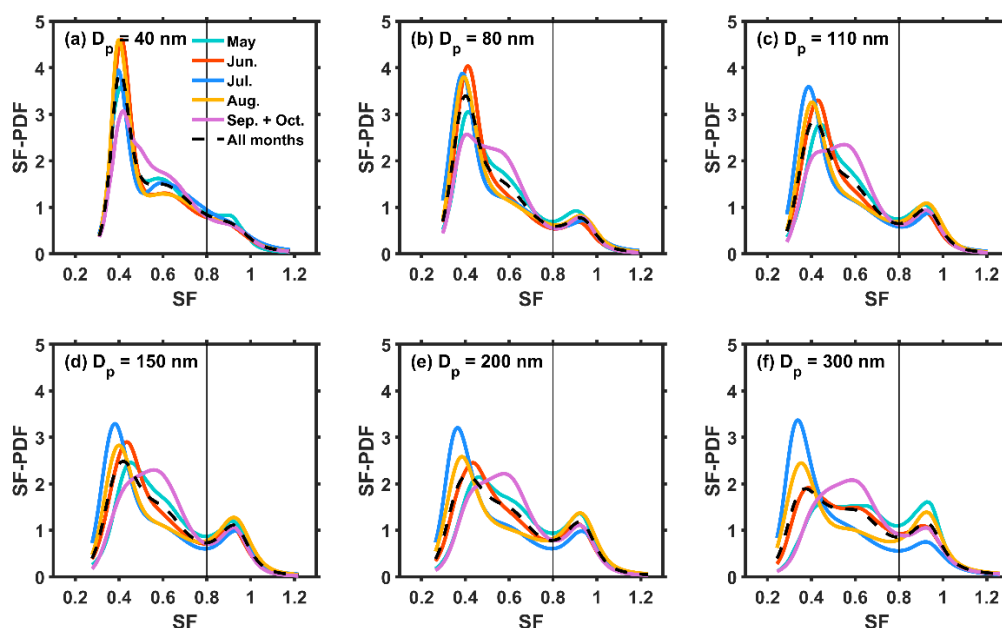
261 degree of internal mixing. These tiny soot particles in nucleation mode are mainly from modern  
 262 vehicle emissions (La Rocca et al., 2015; Hu et al., 2021). Figure 3 also suggests that the fraction  
 263 of NV-mode particles increased with increasing particle size, indicating a higher fraction of  
 264 externally mixed soot particles in accumulation mode. This is related to the primary size of soot  
 265 particles. Some studies suggest that freshly emitted refractory particles (like BC) are primarily in  
 266 accumulation mode. For example, Levy et al. (2013) reported that fresh BC was mostly in the  
 267 150–240 nm size range, while Wu et al. (2017) reported that refractory BC size distribution  
 268 measurements in Beijing peaked at about 200 nm, with a secondary less significant mode at about  
 269 600 nm.



271  
 272 **Figure 3.** Size-resolved mean probability density functions of the shrink factor at different  
 273 wavelengths. VV stands for “very volatile”, SV stands for “slightly volatile”, and NV stands for  
 274 “non-volatile”.

275  
 276 Figure 4a-b shows that VV-mode fractions in the *SF*-PDFs of 40-nm and 80-nm particles were  
 277 higher in warm months than in cold months, indicating that nucleation-mode soot particles were  
 278 more volatile in warm months. Our previous study has shown that new particle formation (NPF)  
 279 events occurred frequently at XT (Y. Wang et al., 2018). Wehner et al. (2009) reported that most  
 280 newly formed matter is composed of organics and sulfate, easily volatilized at 300°C. Li et al. (2011)  
 281 indicated that the tiny soot particles embedded in sulfates could promote particle growth during NPF  
 282 events in the NCP. All this implies that coating by newly formed secondary matter was the possible  
 283 reason for the high volatility of nucleation-mode soot-containing particles in warm months. For  
 284 accumulation-mode (110–300 nm) particles (Fig. 4c-f), monthly changes in *SF*-PDF patterns are  
 285 clearly seen. In general, *SF* peak values of the VV mode were smaller (meaning a thicker coating of  
 286 volatile matter), and fractions of VV-mode particles were higher in warm months (especially in July)

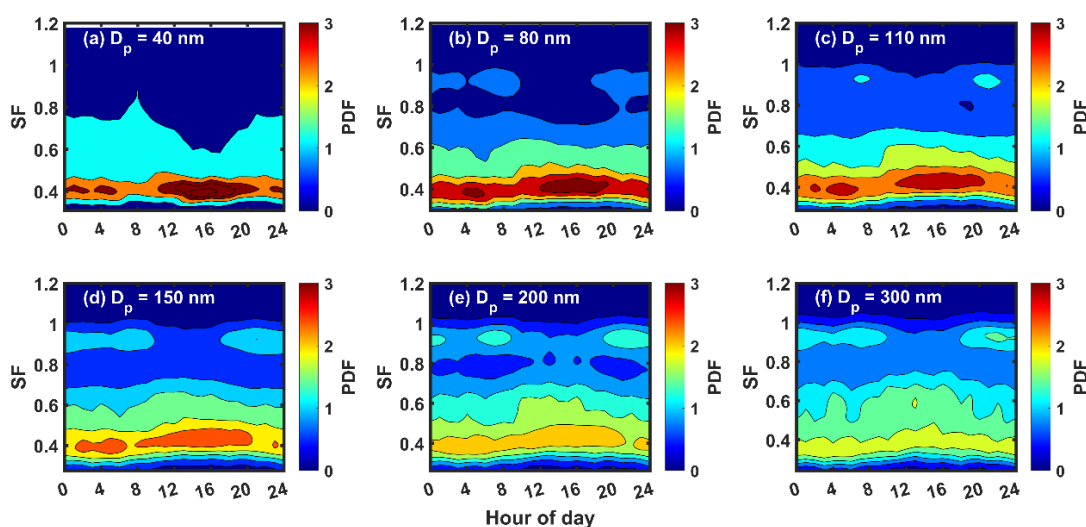
287 than in cold months, indicating that the coating on accumulation-mode soot particles was also  
 288 stronger in warm months than in cold months. As previously mentioned, meteorological conditions  
 289 in warm months (i.e., high  $T$  and RH) were favorable to the particle growth of soot particles through  
 290 atmospheric photochemical and liquid chemical reactions. In cold months (May, September, and  
 291 October), the volatility of accumulation-mode soot-containing particles was relatively lower,  
 292 indicating thinner coating matter on the surfaces of soot particles in the polluted cold environment.  
 293 This is consistent with measurements made at an urban site in Beijing (Yu et al., 2020). Yu et al.  
 294 (2020) also suggests that a more even distribution of  $rBC$  and non- $rBC$  material mass fractions in  
 295 summer than in winter, which may be caused by higher amount of secondary material.  
 296



297  
 298 **Figure 4.** Monthly variations in the mean shrink factor ( $SF$ ) probability distribution functions ( $SF$ -  
 299 PDFs) for particles with diameters of (a) 40 nm, (b) 80 nm, (c) 110 nm, (d) 150 nm, (e) 200 nm,  
 300 and (f) 300 nm.

302 Figure 5 shows diurnal variations in  $SF$ -PDF for different size particles, illustrating the distinct  
 303 diurnal variation patterns of  $SF$ -PDF for nucleation- and accumulation-mode particles. VV-mode  
 304 fractions for 40-nm and 80-nm particles ( $\sim SF = 0.4$ ) increased sharply from around noon into the  
 305 afternoon (Fig. 5a-b). Figure S3 shows that the number concentration of 40-nm and 80-nm particles  
 306 increased quickly due to the influence of NPF events. This further corroborates that newly formed  
 307 particles created during NPF events are the possible coating matter on nucleation-mode soot  
 308 particles. Figure 5c-f suggests that NV-mode fractions in accumulation-mode soot particles ( $\sim SF =$   
 309 0.9) were higher than those in nucleation-mode soot particles and that these fractions became higher  
 310 with increasing particle size. NV-mode fractions in accumulation-mode soot particles clearly

311 increased during the morning and evening rush hours. This suggests that anthropogenic emissions  
 312 have a large impact on the volatility and mixing state of soot particles, especially for accumulation-  
 313 mode soot particles. Previous studies have shown that some of the primary pollutants generated by  
 314 human activities are composed of refractory materials, such as BC (Philippin et al., 2004; Levy et  
 315 al., 2014). An increase in primary refractory particles could weaken the ensemble volatility and  
 316 mixing state of soot particles. Figure 3c-f also shows that the NV-mode fraction in the *SF*-PDF of  
 317 accumulation-mode particles decreased sharply in the daytime, likely caused by the coating effect  
 318 of volatile matter through photochemical reactions.  
 319



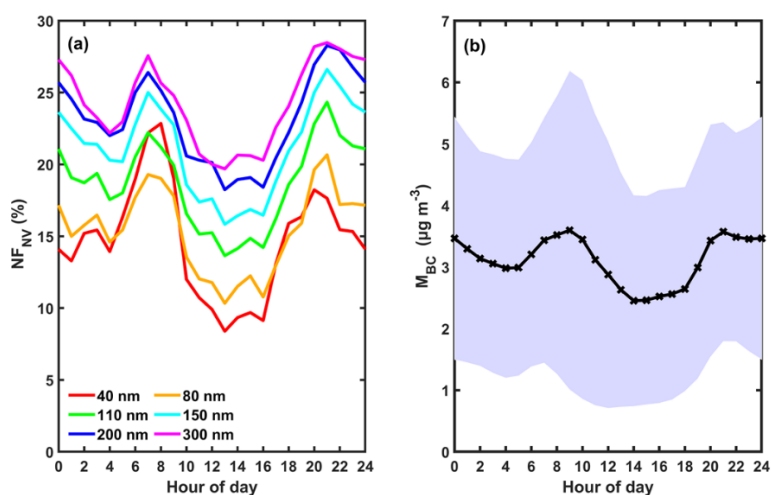
320  
 321 **Figure 5.** Diurnal variations in size-resolved shrink factor (*SF*) probability distribution functions  
 322 (PDFs) for particles with diameters of (a) 40 nm, (b) 80 nm, (c) 110 nm, (d) 150 nm, (e) 200 nm,  
 323 and (f) 300 nm.

324  
 325 In summary, the volatility and mixing state of soot-containing particles were complex at XT  
 326 during the field campaign. Soot-containing particles in the nucleation mode had strong volatility  
 327 and a high degree of internal mixing, likely due to the impact of frequent NPF events that occurred  
 328 during this campaign. The strong volatility and high degree of internal mixing in warm months were  
 329 likely caused by the aging processes of particles. Anthropogenic emissions also had a large impact  
 330 on the volatility and mixing state of soot particles, especially in the accumulation mode. The impacts  
 331 of anthropogenic emissions and secondary chemical reactions on the volatility and mixing state of  
 332 soot particles will be further discussed next.

333  
 334 **3.3 Factors influencing the volatility and mixing state of soot particles**

335 3.3.1 The impact of anthropogenic emissions on the volatility and mixing state of soot  
336 particles

337 As previously discussed, soot particles from anthropogenic emissions were always refractory and  
338 nonvolatile at 300°C. Analyzing the relationship between the number fraction of nonvolatile-mode  
339 particles ( $NF_{NV}$ ,  $SF > 0.8$ ) in  $SF$ -PDFs and  $M_{BC}$  can verify this because BC is the main matter in  
340 soot particles. Figure 6a shows that  $NF_{NV}$  reached two peak values, one during the morning rush  
341 hour at about 08:00 and the other during the evening rush hour at about 20:00.  $M_{BC}$  also reached  
342 two peak values at those same times (Fig. 6b). Overall, the diurnal variation trends of  $NF_{NV}$  for all  
343 sizes and  $M_{BC}$  were similar. This suggests the great impact of anthropogenic BC on the volatility  
344 and mixing state of soot particles.  $NF_{NV}$  decreased quickly after rush hours, especially in the  
345 morning (Fig. 6a), suggesting that the aging processes of primary soot particles were quick at this  
346 heavily polluted site. Cheng et al. (2012) also observed the same phenomenon at a suburban site in  
347 Beijing.

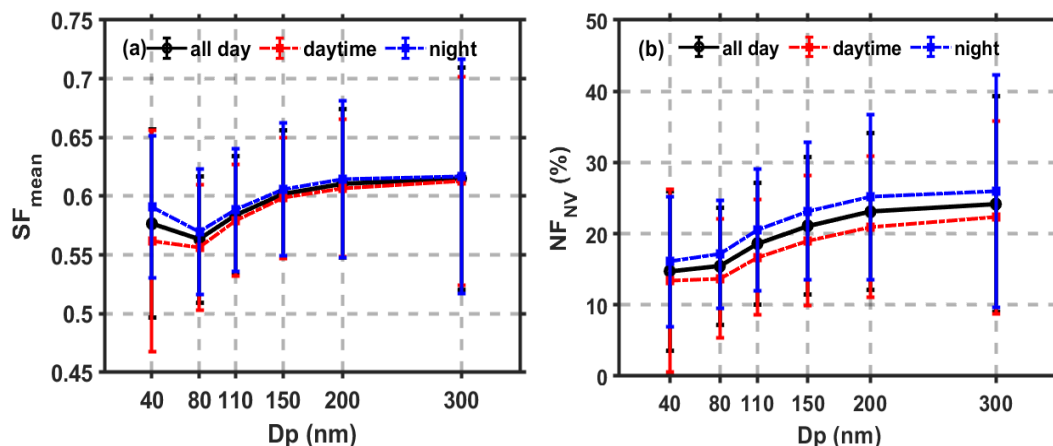


348  
349 **Figure 6.** Diurnal variations in (a) wavelength-dependent, size-resolved number fractions of  
350 nonvolatile particles ( $NF_{NV}$ ), and (b) mass concentration of black carbon ( $M_{BC}$ ). The purple,  
351 shaded area shows the standard deviations of  $M_{BC}$ .

352  
353 3.3.2 The impact of aging processes on the volatility and mixing state of soot-containing  
354 particles

355 Lower  $SF_{\text{mean}}$  values mean stronger aerosol volatility, indicating a larger coating depth of volatile  
356 matter on soot particles. Figure 7a suggests that volatility is stronger during daytime than at night  
357 (i.e., a lower  $SF_{\text{mean}}$ ), particularly for 40-nm particles. This illustrates the large impact of  
358 photochemical reactions on the volatility and mixing state of soot particles. Figure 7a also suggests  
359 that the  $SF_{\text{mean}}$  of 80-nm particles was lower than that of 40-nm particles. Wang et al. (2018) suggests  
360 that aerosol hygroscopicity of 40-nm particles is larger than that of 80-nm particles during the

361 daytime at this site. These indicate the great impact of photochemical reactions on the  
 362 physicochemical properties of nucleation-mode particles. Inversely,  $SF_{\text{mean}}$  increased with  
 363 increasing particle size in the accumulation mode (110–300 nm), suggesting weaker volatility and  
 364 a smaller coating depth for larger accumulation-mode soot particles.  
 365



366  
 367 **Figure 7.** (a) Size-resolved ensemble mean shrink factors ( $SF_{\text{mean}}$ ) and (b) size-resolved number  
 368 fractions of nonvolatile particles ( $NF_{\text{NV}}$ ) during the 24-hr day (black solid lines), during daytime  
 369 (red dotted lines), and during nighttime (blue dotted lines). The error bars denote standard deviations.

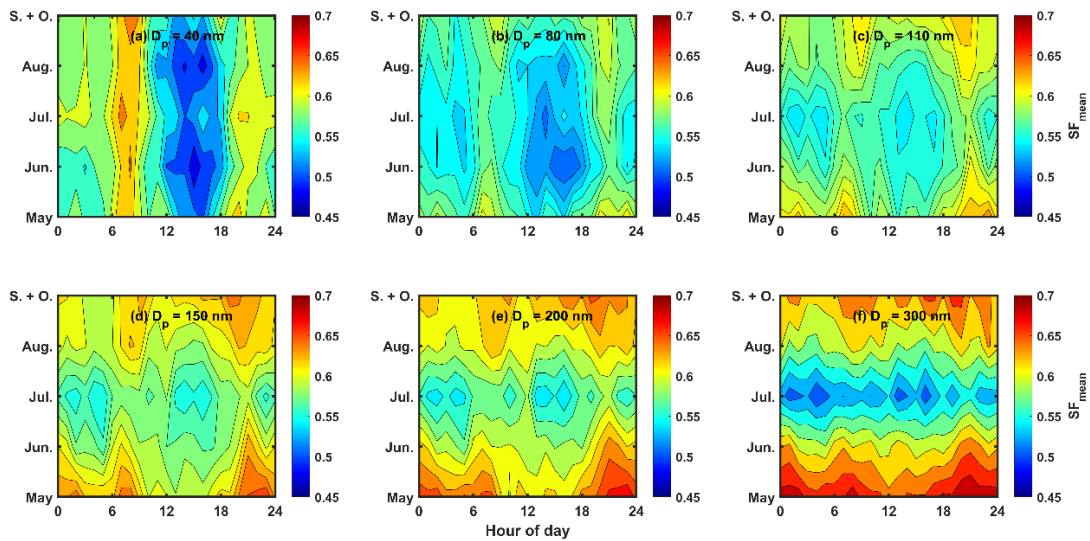
370 Figure 8 shows the diurnal variation in  $SF_{\text{mean}}$  in different months for different particle sizes.  
 371 Figure 8a-b shows that the  $SF_{\text{mean}}$  of 40-nm and 80-nm particles clearly increased during the  
 372 morning and evening rush hours in all months. However, the  $SF_{\text{mean}}$  of 40-nm and 80-nm particles  
 373 decreased sharply in the afternoon. This suggests that the volatility of nucleation-mode soot-  
 374 containing particles was easily influenced by anthropogenic emissions during rush hours and  
 375 photochemical reactions in the daytime. The diurnal variation patterns of  $SF_{\text{mean}}$  (Fig. 8c-f) in the  
 376 accumulation mode were diverse in different months. The  $SF_{\text{mean}}$  in warm months was usually lower  
 377 than in cold months, indicating a larger impact of aging processes on the volatility of accumulation-  
 378 mode soot-containing particles in warm months. Figure 8c-f also shows that the  $SF_{\text{mean}}$  in  
 379 accumulation mode was lowest in July. This suggests that high  $T$ , high RH, and the stable  
 380 atmospheric environment in July were conducive to the coating of secondary matter on  
 381 accumulation-mode soot particles, a possible reason for the high aerosol pollution levels in July.  
 382 Moreover, Fig. 8 suggests that monthly variations in  $SF_{\text{mean}}$  became larger with increasing particle  
 383 size. The seasonal variation in the coating effect should thus be considered when modeling  
 384 physicochemical properties of soot particles, especially larger particles.

385 To further investigate the impact of aging processes on the mixing state of soot particles, size-  
 386 resolved  $NF_{\text{NV}}$  in the daytime and at night were compared (Fig. 7b).  $NF_{\text{NV}}$  was always lower in the  
 387 daytime than at night, meaning that the fraction of externally mixed soot particles in the daytime

388 was lower. This further indicates that photochemical reactions in the daytime can transform  
 389 externally mixed soot particles into internally mixed soot particles. Figure 7b also shows that  $NF_{NV}$   
 390 increased with increasing particle size, meaning a higher degree of external mixing of larger  
 391 particles. This suggests that the degree of external mixing was higher for accumulation-mode soot  
 392 particles than nucleation-mode particles.

393 The diurnal variation patterns of  $NF_{NV}$  (Fig. S4) and  $SF_{\text{mean}}$  (Fig. 8) in different months were  
 394 similar. Externally mixed soot particles increased during the morning and evening rush hours due  
 395 to enhanced anthropogenic emissions. Monthly differences in  $NF_{NV}$  increased with increasing  
 396 particle size. Figure S4 also shows a lower number fraction of externally mixed soot particles (i.e.,  
 397 a smaller  $NF_{NV}$ ) in warm months than in cold months.

398 These results illustrate the distinct volatilities and mixing states of soot particles between the  
 399 nucleation and accumulation modes. A lower degree of external mixing and thicker coating depth  
 400 in nucleation-mode particles exists. It is thus important to quantify the impact of the coating effect  
 401 for nucleation-mode soot particles when studying aerosol physicochemical properties. The next  
 402 section analyzes the coating depth and its influencing factors.  
 403



404

405 **Figure 8.** Diurnal variations in ensemble mean shrink factor ( $SF_{\text{mean}}$ ) in different months for  
 406 different particle sizes.

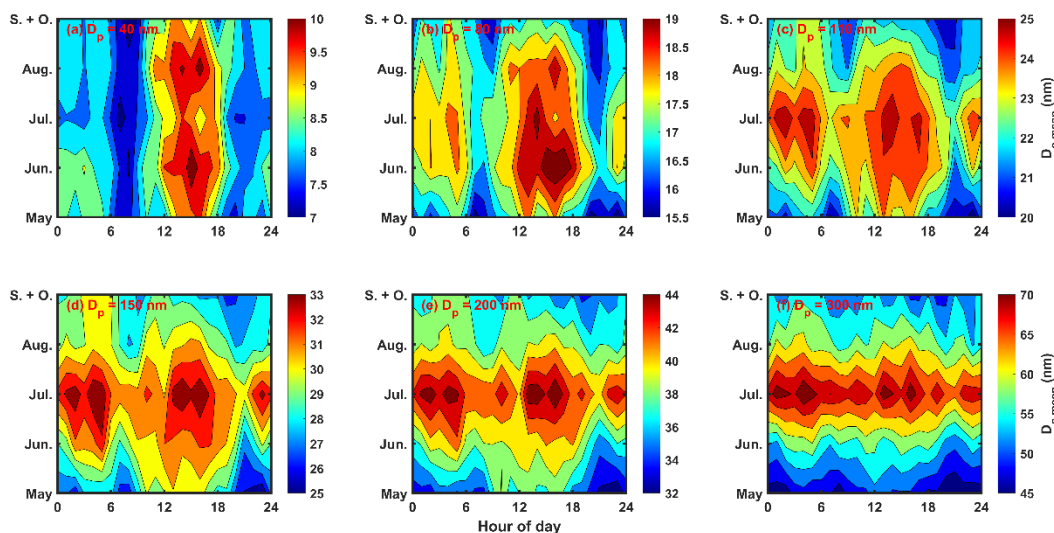
407

### 408 3.4 The coating depth of secondary matter on soot particles

409 The ensemble mean coating depth on soot particles ( $D_{c,\text{mean}}$ ) can be calculated using Eq. (4).  
 410 Figure 9 shows diurnal variations in  $D_{c,\text{mean}}$  in different months for different particle sizes. The  
 411 diurnal variation patterns of  $D_{c,\text{mean}}$  for nucleation-mode and accumulation-mode soot particles  
 412 differ greatly. The diurnal variation patterns of  $D_{c,\text{mean}}$  in different months were similar for



413 nucleation-mode soot particles (40-nm and 80-nm particles) but not for accumulation-mode soot  
 414 particles (110–300-nm particles). The enhancement of  $D_{c,mean}$  in the daytime occurred in all months  
 415 for nucleation-mode soot particles but only in the warm months for accumulation-mode soot  
 416 particles. At night, the enhancement of  $D_{c,mean}$  for accumulation-mode soot particles was strong,  
 417 especially in warm months. However, it was weak for nucleation-mode soot particles. These all  
 418 imply large differences in  $D_{c,mean}$  in different months for nucleation-mode and accumulation-mode  
 419 soot particles, likely caused by variations in meteorological conditions and aerosol pollution levels.  
 420



421  
 422 **Figure 9.** Diurnal variations in ensemble mean coating depth ( $D_{c,mean}$ ) on soot particles in different  
 423 months for different particle sizes. Note that the color bars have different ranges of values in each  
 424 panel.

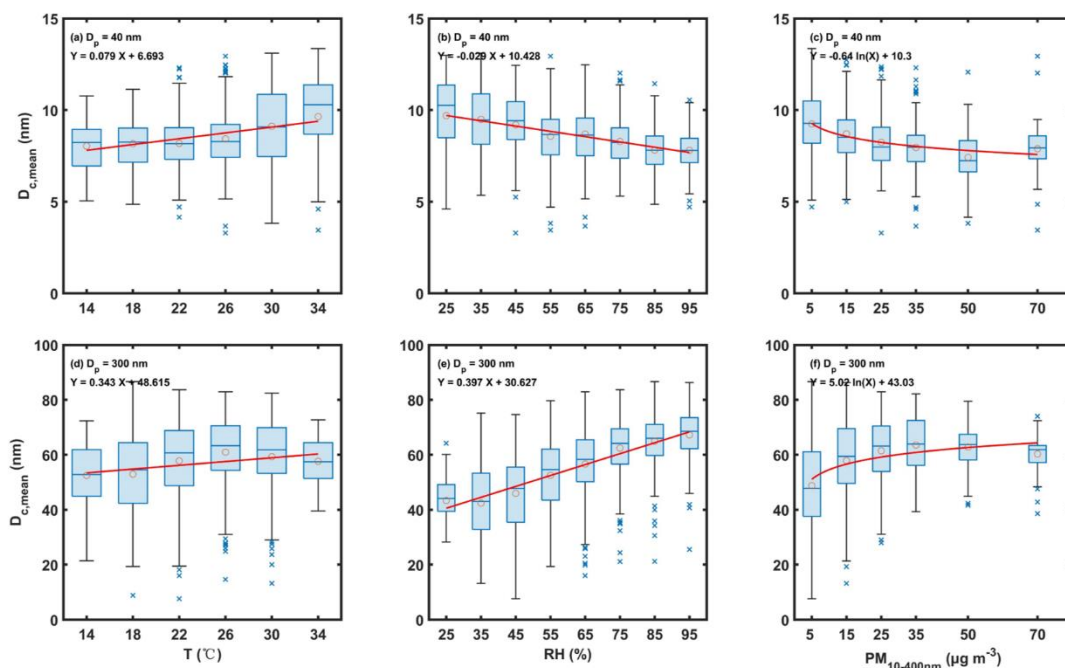
425  
 426 The relationships between  $D_{c,mean}$  and several possible influencing factors ( $T$ , RH, and  $PM_{10-400nm}$ )  
 427 were further analyzed (Fig. 10). Figures 10a and 10d show positive correlations between  
 428  $D_{c,mean}$  and  $T$  for both nucleation-mode and accumulation-mode particles (represented by 40-nm and  
 429 300-nm particles, respectively). This is consistent with the results shown in Fig. 7. Zhang et al.  
 430 (2021) also indicated that warm environments were favorable to the aging of  $rBC$ . The high daytime  
 431  $T$  was conducive to the aging of soot particles caused by strong photochemical reactions. However,  
 432 the relationships between RH and  $D_{c,mean}$  (Figs. 9b and 9e) and between  $PM_{10-400nm}$  and  $D_{c,mean}$  (Figs.  
 433 9c and 9f) were inverse between nucleation- and accumulation-mode soot particles.

434 Figure 9 depicts a linear relationship between  $D_{c,mean}$  and RH, while a logarithmic relationship  
 435 between  $D_{c,mean}$  and  $PM_{10-400nm}$ .  $D_{c,mean}$  in the nucleation mode decreased with increasing RH and  
 436  $PM_{10-400nm}$  for nucleation-mode soot particles (Fig. 9b-c). This suggests that high ambient RH and  
 437 severe aerosol pollution events could inhibit the coating of nucleation-mode soot particles. Previous  
 438 studies have reported that aerosol pollution events were generally associated with high RH in the

439 NCP (G. Wang et al., 2016; Z. Wu et al., 2018). This suggests that highly polluted environments  
 440 with high ambient RH are not beneficial to the formation of new particles, leading to the weak  
 441 coating on nucleation-mode soot particles. However,  $D_{c,mean}$  in the accumulation mode increased  
 442 with increasing RH and  $PM_{10-400nm}$  (Fig. 9e-f). This suggests that highly polluted environments with  
 443 high ambient RH favor the growth of accumulation-mode soot particles by coating. This is possibly  
 444 related to enhanced liquid-phase chemical reactions under these environmental conditions.  
 445 Considering that accumulation-mode particles are the dominant components of  $PM_{10-400nm}$ , this  
 446 further implies that the coating on soot particles is important to the formation of heavy aerosol  
 447 pollution events. Y. Wang et al. (2019) indicated that the properties of ultrafine- and accumulation-  
 448 mode particles were distinct in clean and polluted urban environments due to the different particle  
 449 formation and growth processes. This study further indicates that it is also distinct in the aging of  
 450 soot particles.

451 In summary, high ambient  $T$  and RH levels appeared to promote the coating growth of  
 452 accumulation-mode soot particles in highly polluted environments. High ambient  $T$  but low RH  
 453 were beneficial to the coating growth of nucleation-mode soot particles in less polluted  
 454 environments.

455



456

457 **Figure 10.** Relationships between ensemble mean coating depth ( $D_{c,mean}$ ) and ambient  $T$  (a, d) and  
 458 RH (b, e), and  $PM_{10-400nm}$  (c, f) for 40-nm (top panels) and 300-nm (bottom panels) particles. The  
 459 circles show the mean  $D_{c,mean}$  with boxes showing the 25th, 50th, and 75th percentiles and  
 460 extremities show the 5th and 95th percentiles. Red lines show the linear or logarithmic fitting lines  
 461 through the data, and best-fit relations are given in each panel.

462

#### 463 4. Summary and conclusions

464 Soot particles containing most of the black carbon (BC) in the atmosphere are the most  
465 important light-absorbing carbonaceous particles. Investigating the mixing state of soot particles in  
466 the field is crucial to accurately model aerosol absorption and reduce the uncertainty of radiative  
467 forcing caused by aerosols in climate models.

468 Here, over five months of volatility tandem differential mobility analyzer (VTDMA) data  
469 collected at a heavily polluted suburban site (Xingtai, or XT) from May to October of 2016 were  
470 used to study the volatility and mixing state of size-resolved soot particles and their influencing  
471 factors. Ambient meteorological variables [temperature ( $T$ ), relative humidity (RH), and winds]  
472 varied between the warm (June, July, and August) and cold (May, September, and October) months  
473 of the field campaign. Variations in meteorological parameters could induce various aerosol aging  
474 processes and different levels of aerosol pollution, largely impacting the volatility and mixing state  
475 of soot particles.

476 The retrieved probability density function of the shrink factor ( $SF$ -PDF) at XT had three modes,  
477 demonstrating that the volatility and mixing state of soot-containing particles were more complex  
478 at XT than at other sites in the North China Plain. Compared with accumulation-mode soot-  
479 containing particles, nucleation-mode soot-containing particles were more volatile and had a higher  
480 degree of internal mixing. The diurnal variation patterns of  $SF$ -PDFs suggest that coating by newly  
481 formed materials was the possible reason for the enhanced volatility of nucleation-mode soot-  
482 containing particles in the daytime. Moreover, the enhanced nocturnal secondary aerosol formation  
483 was responsible for the enhanced volatility of accumulation-mode soot-containing particles in the  
484 nighttime. The ensemble mean  $SF$  ( $SF_{\text{mean}}$ ) was size dependent and varied monthly. The monthly  
485 variations in  $SF_{\text{mean}}$  became larger with increasing particle size, implying a stronger seasonal  
486 variation of the coating effect on soot particles for larger-sized particles.

487 The similar diurnal variation trends of the number fraction of nonvolatile mode particles ( $NF_{\text{NV}}$ )  
488 in  $SF$ -PDFs and the mass concentration of BC ( $M_{\text{BC}}$ ) suggest that human activities had a negative  
489 influence on the volatility and degree of internal mixing of soot particles, especially for  
490 accumulation-mode soot-containing particles. In general, less externally mixed soot particles (i.e.,  
491 a smaller  $NF_{\text{NV}}$ ) were present in warm months than in cold months.  $NF_{\text{NV}}$  was always lower in the  
492 daytime than at night, suggesting a lower fraction of externally mixed soot particles in the daytime.  
493 This suggests that daytime photochemical reactions may promote the transformation of externally  
494 mixed soot particles into internally mixed soot particles. Moreover,  $NF_{\text{NV}}$  increased with increasing  
495 particle size, meaning a higher degree of external mixing for larger-sized particles. This also  
496 suggests that the degree of external mixing was higher for accumulation-mode soot particles than

497 for nucleation-mode soot particles.

498 To explore factors influencing soot-particle volatility and mixing state, the ensemble mean  
499 coating depth ( $D_{c,mean}$ ) of volatile matter on soot particles was investigated.  $D_{c,mean}$  was thicker in  
500 warm months than in cold months, even though aerosol pollution was heavier in cold months. In  
501 warm months,  $D_{c,mean}$  was larger in July than in other months, likely because high  $T$ , high RH, and  
502 the stable atmospheric environment in July were conducive to the coating effect on soot particles.  
503 The relationships between  $D_{c,mean}$  and possible influencing factors (i.e.,  $T$ , RH, and  $PM_{10-400nm}$ ) show  
504 that high ambient  $T$  and RH in a polluted environment promoted the coating growth of  
505 accumulation-mode soot particles. High ambient  $T$  but low RH in a clean environment was  
506 beneficial to the coating growth of nucleation-mode soot particles.

507 These results demonstrate great differences in the volatility and mixing state between nucleation-  
508 and accumulation-mode soot particles. The impact of anthropogenic emissions on the volatility and  
509 mixing state of soot-containing particles was clearly seen, especially for accumulation-mode soot-  
510 containing particles. The monthly variations in meteorological conditions and aerosol pollution  
511 levels may induce different aerosol aging processes, strongly impacting the volatility and mixing  
512 state of soot-containing particles. This study suggests that differences between the mixing states of  
513 nucleation- and accumulation-mode soot particles and their influencing factors should be considered  
514 in climate models.

515

516 *Acknowledgement.* This work was funded by the National Natural Science Foundation of China  
517 (NSFC) research project (grant no. 42030606, 42005067, 92044303), the National Key R&D  
518 Program of the Ministry of Science and Technology, China (grant no. 2017YFC1501702), and the  
519 Open Fund of State Key Laboratory of Remote Sensing Science (grant no. 202015). We also thank  
520 all participants in the campaign for their tireless work and cooperation.

521

522 *Data availability.* The measurement data from the field experiment used in this study are available  
523 from the first author upon request (yuyingwang@nuist.edu.cn).

524

525 *Author contributions.* YW conceived the study and led the overall scientific questions. YW,  
526 RH, and QW processed the measurement data and prepared this paper. ZL, MC copyedited the  
527 article. Other co-authors participated in the implementation of this experiment and the discussion  
528 of this paper.

529

530 *Competing interests.* The authors declare that they have no conflict of interest.

531

532

533

## 534 **References**

535 Adachi, K., Sedlacek, A. J., Kleinman, L., Chand, D., Hubbe, J. M., and Buseck, P. R.: Volume changes  
536 upon heating of aerosol particles from biomass burning using transmission electron microscopy,  
537 *Aerosol Sci. Tech.*, 52, 46-56, <https://doi.org/10.1080/02786826.2017.1373181>, 2018.

538 Adachi, K., Sedlacek, A. J., Kleinman, L., Springston, S. R., Wang, J., Chand, D., Hubbe, J. M., Shilling,  
539 J. E., Onasch, T. B., Kinase, T., Sakata, K., Takahashi, Y., and Buseck, P. R.: Spherical tarball  
540 particles form through rapid chemical and physical changes of organic matter in biomass-burning  
541 smoke, *Proceedings of the National Academy of Sciences*, 116, 19336-19341,  
542 <https://doi.org/10.1073/pnas.1900129116>, 2019.

543 Bellouin, N., Quaas, J., Gryspeerdt, E., Kinne, S., Stier, P., Watson-Parris, D., Boucher, O., Carslaw, K.  
544 S., Christensen, M., Daniau, A. L., Dufresne, J. L., Feingold, G., Fiedler, S., Forster, P., Gettelman,  
545 A., Haywood, J. M., Lohmann, U., Malavelle, F., Mauritsen, T., McCoy, D. T., Myhre, G.,  
546 Mülmenstädt, J., Neubauer, D., Possner, A., Rugenstein, M., Sato, Y., Schulz, M., Schwartz, S. E.,  
547 Sourdeval, O., Storelvmo, T., Toll, V., Winker, D., and Stevens, B.: Bounding global aerosol radiative  
548 forcing of climate change, *Rev. Geophys.*, 58, e2019R-e2660R, 2020.

549 Bond, T. C., Doherty, S. J., Fahey, D. W., Forster, P. M., Berntsen, T., DeAngelo, B. J., Flanner, M. G.,  
550 Ghan, S., Kärcher, B., Koch, D., Kinne, S., Kondo, Y., Quinn, P. K., Sarofim, M. C., Schultz, M. G.,  
551 Schulz, M., Venkataraman, C., Zhang, H., Zhang, S., Bellouin, N., Guttikunda, S. K., Hopke, P. K.,  
552 Jacobson, M. Z., Kaiser, J. W., Klimont, Z., Lohmann, U., Schwarz, J. P., Shindell, D., Storelvmo, T.,  
553 Warren, S. G., and Zender, C. S.: Bounding the role of black carbon in the climate system: A scientific  
554 assessment, *J. Geophys. Res. Atmos.*, 118, 5380-5552, <https://doi.org/10.1002/jgrd.50171>, 2013.

555 Cheng, Y. F., Berghof, M., Garland, R. M., Wiedensohler, A., Wehner, B., Müller, T., Su, H., Zhang, Y.  
556 H., Achtert, P., Nowak, A., Pöschl, U., Zhu, T., Hu, M., and Zeng, L. M.: Influence of soot mixing  
557 state on aerosol light absorption and single scattering albedo during air mass aging at a polluted  
558 regional site in northeastern China, *J. Geophys. Res. Atmos.*, 114, 2009.

559 Cheng, Y. F., Su, H., Rose, D., Gunthe, S. S., Berghof, M., Wehner, B., Achtert, P., Nowak, A.,  
560 Takegawa, N., Kondo, Y., Shiraiwa, M., Gong, Y. G., Shao, M., Hu, M., Zhu, T., Zhang, Y. H.,  
561 Carmichael, G. R., Wiedensohler, A., Andreae, M. O., and Pöschl, U.: Size-resolved measurement of  
562 the mixing state of soot in the megacity Beijing, China: diurnal cycle, aging and parameterization,  
563 *Atmos. Chem. Phys.*, 12, 4477-4491, 2012.

564 Cheung, H. H., Tan, H., Xu, H., Li, F., Wu, C., Yu, J. Z., and Chan, C. K.: Measurements of non-volatile  
565 aerosols with a VTDMA and their correlations with carbonaceous aerosols in Guangzhou, China,  
566 *Atmos. Chem. Phys.*, 16, 8431-8446, 2016.

567 Christensen, M., Gettelman, A., Cermak, J., Dagan, G., Diamond, M., Douglas, A., Feingold, G.,  
568 Glassmeier, F., Goren, T., Grosvenor, D., Gryspeerdt, E., Kahn, R., Li, Z., Ma, P. L., Malavelle, F.,  
569 McCoy, I., McCoy, D., McFarquhar, G., Mülmenstädt, J., Pal, S., Possner, A., Povey, A., Quaas, J.,  
570 Rosenfeld, D., Schmidt, A., Schrödner, R., Sorooshian, A., Stier, P., Toll, V., Watson-Parris, D.,  
571 Wood, R., Yang, M., and Yuan, T.: Opportunistic experiments to constrain aerosol effective radiative

572 forcing, *Atmos. Chem. Phys. Discuss.*, 2021, 1-60, 2021.

573 Gustafsson, Ö., and Ramanathan, V.: Convergence on climate warming by black carbon aerosols, *Proc.*  
574 *Natl. Acad. Sci. U.S.A.*, 113, 4243, <https://doi.org/10.1073/pnas.1603570113>, 2016.

575 Hong, J., Äijälä, M., Häme, S. A. K., Hao, L., Duplissy, J., Heikkinen, L. M., Nie, W., Mikkilä, J.,  
576 Kulmala, M., Prisle, N. L., Virtanen, A., Ehn, M., Paasonen, P., Worsnop, D. R., Riipinen, I., Petäjä,  
577 T., and Kerminen, V. M.: Estimates of the organic aerosol volatility in a boreal forest using two  
578 independent methods, *Atmos. Chem. Phys.*, 17, 4387-4399, [https://doi.org/10.5194/acp-17-4387-](https://doi.org/10.5194/acp-17-4387-2017)  
579 2017, 2017.

580 Hossain, A. M. M. M., Park, S., Kim, J. S., and Park, K.: Volatility and mixing states of ultrafine particles  
581 from biomass burning, *J. Hazard. Mater.*, 205-206, 189-197, 2012.

582 [Hu, Z., Lu, Z., Zhang, H., Song, B., and Quan, Y.: Effect of oxidation temperature on oxidation reactivity](#)  
583 [and nanostructure of particulate matter from a China VI GDI vehicle, \*Atmos. Environ.\*, 256, 118461,](#)  
584 <https://doi.org/10.1016/j.atmosenv.2021.118461>, 2021.

585 IPCC: Climate change 2021: The Physical Science Basis, sixth assessment of the Inter-governmental  
586 Panel on Climate Change, *in press*, 2021.

587 Kuniyal, J. C., and Guleria, R. P.: The current state of aerosol-radiation interactions: a mini review, *J.*  
588 *Aerosol Sci.*, 130, 45-54, 2019.

589 [La Rocca, A., Bonatesta, F., Fay, M. W., and Campanella, F.: Characterisation of soot in oil from a](#)  
590 [gasoline direct injection engine using Transmission Electron Microscopy, \*Tribol. Int.\*, 86, 77-84,](#)  
591 <https://doi.org/10.1016/j.triboint.2015.01.025>, 2015.

592 Levy, M. E., Zhang, R., Khalizov, A. F., Zheng, J., Collins, D. R., Glen, C. R., Yuan, W., Yu, X. Y.,  
593 Winston, L., and Jayne, J. T.: Measurements of submicron aerosols in Houston, Texas during the 2009  
594 SHARP field campaign, *J. Geophys. Res. Atmos.*, 118, 10,518-10,534,  
595 <https://doi.org/10.1002/jgrd.50785>, 2013.

596 Levy, M. E., Zhang, R., Zheng, J., Tan, H., Wang, Y., Molina, L. T., Takahama, S., Russell, L. M., and  
597 Li, G.: Measurements of submicron aerosols at the California - Mexico border during the Cal-Mex  
598 2010 field campaign, *Atmos. Environ.*, 88, 308-319, 2014. Li, Z., Wang, Y., Guo, J., Zhao, C., Cribb,  
599 M. C., Dong, X., Fan, J., Gong, D., Huang, J., Jiang, M., Jiang, Y., Lee, S. S., Li, H., Li, J., Liu, J.,  
600 Qian, Y., Rosenfeld, D., Shan, S., Sun, Y., Wang, H., Xin, J., Yan, X., Yang, X., Yang, X., Zhang, F.,  
601 and Zheng, Y.: East Asian Study of Tropospheric Aerosols and their Impact on Regional Clouds,  
602 Precipitation, and Climate (EAST-AIR<sub>CPC</sub>), *J. Geophys. Res. Atmos.*, 124, 13,026-13,054,  
603 <https://doi.org/10.1029/2019JD030758>, 2019.

604 [Li, W. J., Zhang, D. Z., Shao, L. Y., Zhou, S. Z., and Wang, W. X.: Individual particle analysis of aerosols](#)  
605 [collected under haze and non-haze conditions at a high-elevation mountain site in the North China](#)  
606 [plain, \*Atmos. Chem. Phys.\*, 11, 11733-11744, 10.5194/acp-11-11733-2011, 2011.](#)

607 Drinovec, L., Močnik, G., Zotter, P., Prévôt, A. S. H., Ruckstuhl, C., Coz, E., Rupakheti, M., Sciare, J.,  
608 Müller, T., Wiedensohler, A., and Hansen, A. D. A.: The "dual-spot" Aethalometer: an improved  
609 measurement of aerosol black carbon with real-time loading compensation, *Atmos. Meas. Tech.*, 8,  
610 1965-1979, <https://doi.org/10.5194/amt-8-1965-2015>, 2015.

611 Novakov, T., Ramanathan, V., Hansen, J. E., Kirchstetter, T. W., Sato, M., Sinton, J. E., and Sathaye, J.  
612 A.: Large historical changes of fossil-fuel black carbon aerosols, *Geophys. Res. Lett.*, 30,  
613 <https://doi.org/10.1029/2002GL016345>, 2003.

614 Peng, J., Hu, M., Guo, S., Du, Z., Zheng, J., Shang, D., Zamora, M. L., Zeng, L., Shao, M., and Wu, Y.:  
615 Markedly enhanced absorption and direct radiative forcing of black carbon under polluted urban

616 environments, *Proc. Natl. Acad. Sci. U.S.A.*, 113, 4266-4271, 2016.

617 Peng, J., Hu, M., Shang, D., Wu, Z., Du, Z., Tan, T., Wang, Y., Zhang, F., and Zhang, R.: Explosive  
618 secondary aerosol formation during severe haze in the North China Plain, *Environ. Sci. Technol.*, 55,  
619 2189-2207, <https://doi.org/10.1021/acs.est.0c07204>, 2021.

620 Philippin, S., Wiedensohler, A., and Stratmann, F.: Measurements of non-volatile fractions of pollution  
621 aerosols with an eight-tube volatility tandem differential mobility analyzer (VTDMA-8), *J. Aerosol*  
622 *Sci.*, 35, 185-203, <https://doi.org/10.1016/j.jaerosci.2003.07.004>, 2004.

623 Ramana, M. V., Ramanathan, V., Feng, Y., Yoon, S., Kim, S., Carmichael, G. R., and Schauer, J. J.:  
624 Warming influenced by the ratio of black carbon to sulphate and the black-carbon source, *Nat. Geosci.*,  
625 3, 542-545, <https://doi.org/10.1038/ngeo918>, 2010.

626 Ren, R., Li, Z., Yan, P., Wang, Y., Wu, H., Cribb, M., Wang, W., Jin, X., Li, Y., and Zhang, D.:  
627 Measurement report: the effect of aerosol chemical composition on light scattering due to the  
628 hygroscopic swelling effect, *Atmos. Chem. Phys.*, 21, 9977-9994, 2021.

629 Seinfeld, J. H., Bretherton, C., Carslaw, K. S., Coe, H., DeMott, P. J., Dunlea, E. J., Feingold, G., Ghan,  
630 S., Guenther, A. B., Kahn, R., Kraucunas, I., Kreidenweis, S. M., Molina, M. J., Nenes, A., Penner, J.  
631 E., Prather, K. A., Ramanathan, V., Ramaswamy, V., Rasch, P. J., Ravishankara, A. R., Rosenfeld,  
632 D., Stephens, G., and Wood, R.: Improving our fundamental understanding of the role of aerosol-  
633 cloud interactions in the climate system, *Proc. Natl. Acad. Sci. U.S.A.*, 113, 5781, 2016.

634 Stolzenburg, M. R., and McMurry, P. H.: TDMAFIT user's manual, University of Minnesota,  
635 Department of Mechanical Engineering, Particle Technology Laboratory, Minneapolis, 1-61, 1988.

636 Stolzenburg, M. R., and McMurry, P. H.: Equations governing single and tandem DMA configurations  
637 and a new lognormal approximation to the transfer function, *Aerosol Sci. Tech.*, 42, 421-432, 2008.

638 Swietlicki, E., Hansson, H. C., Hämeri, K., Svenningsson, B., Massling, A., Mcfiggans, G., McMurry, P.  
639 H., Petäjä, T., Tunved, P., Gysel, M., Topping, D., Weingartner, E., Baltensperger, U., Rissler, J.,  
640 Wiedensohler, A., and Kulmala, M.: Hygroscopic properties of submicrometer atmospheric aerosol  
641 particles measured with H-TDMA instruments in various environments—a review, *Tellus B: Chem.*  
642 *Phys. Meteor.*, 60, 432-469, <https://doi.org/10.1111/j.1600-0889.2008.00350.x>, 2008.

643 Twohy, C. H., Coakley Jr., J. A., and Tahnk, W. R.: Effect of changes in relative humidity on aerosol  
644 scattering near clouds, *J. Geophys. Res. Atmos.*, 114, 2009.

645 Wang, G., Zhang, R., Gomez, M. E., Yang, L., Zamora, M. L., Hu, M., Lin, Y., Peng, J., Guo, S., and  
646 Meng, J.: Persistent sulfate formation from London Fog to Chinese haze, *Proc. Natl. Acad. Sci. U.S.A.*,  
647 113, 13,630-13,635, 2016.

648 Wang, J., Liu, D., Ge, X., Wu, Y., Shen, F., Chen, M., Zhao, J., Xie, C., Wang, Q., Xu, W., Zhang, J.,  
649 Hu, J., Allan, J., Joshi, R., Fu, P., Coe, H., and Sun, Y.: Characterization of black carbon-containing  
650 fine particles in Beijing during wintertime, *Atmos. Chem. Phys.*, 19, 447-458,  
651 <https://doi.org/10.5194/acp-19-447-2019>, 2019.

652 Wang, Y., Zhang, F., Li, Z., Tan, H., Xu, H., Ren, J., Zhao, J., Du, W., and Sun, Y.: Enhanced  
653 hydrophobicity and volatility of submicron aerosols under severe emission control conditions in  
654 Beijing, *Atmos. Chem. Phys.*, 17, 5239-5251, <https://doi.org/10.5194/acp-17-5239-2017>, 2017.

655 Wang, Y., Li, Z., Zhang, Y., Du, W., Zhang, F., Tan, H., Xu, H., Fan, T., Jin, X., Fan, X., Dong, Z.,  
656 Wang, Q., and Sun, Y.: Characterization of aerosol hygroscopicity, mixing state, and CCN activity at  
657 a suburban site in the central North China Plain, *Atmos. Chem. Phys.*, 18, 11,739-11,752,  
658 <https://doi.org/10.5194/acp-18-11739-2018>, 2018.



659 Wang, Y., Li, Z., Zhang, R., Jin, X., Xu, W., Fan, X., Wu, H., Zhang, F., Sun, Y., Wang, Q., Cribb, M.,  
660 and Hu, D.: Distinct ultrafine- and accumulation-mode particle properties in clean and polluted urban  
661 environments, *Geophys. Res. Lett.*, 46, 10,918-10,925, <https://doi.org/10.1029/2019GL084047>, 2019.

662 Wang, Y., Wang, J., Li, Z., Jin, X., Sun, Y., Cribb, M., Ren, R., Lv, M., Wang, Q., Gao, Y., Hu, R.,  
663 Shang, Y., and Gong, W.: Contrasting aerosol growth potential in the northern and central-southern  
664 regions of the North China Plain: implications for combating regional pollution, *Atmos. Environ.*,  
665 267, 118723, <https://doi.org/10.1016/j.atmosenv.2021.118723>, 2021.

666 Wehner, B., Berghof, M., Cheng, Y. F., Achtert, P., Birmili, W., Nowak, A., Wiedensohler, A., Garland,  
667 R. M., Pöschl, U., and Hu, M.: Mixing state of nonvolatile aerosol particle fractions and comparison  
668 with light absorption in the polluted Beijing region, *J. Geophys. Res. Atmos.*, 114, 85-86, 2009.

669 Wu, Y., Wang, X., Tao, J., Huang, R., Tian, P., Cao, J., Zhang, L., Ho, K. F., Han, Z., and Zhang, R.:  
670 Size distribution and source of black carbon aerosol in urban Beijing during winter haze episodes,  
671 *Atmos. Chem. Phys.*, 17, 7965-7975, <https://doi.org/10.5194/acp-17-7965-2017>, 2017.

672 Wu, Z., Wang, Y., Tan, T., Zhu, Y., Li, M., Shang, D., Wang, H., Lu, K., Guo, S., Zeng, L., and Zhang,  
673 Y.: Aerosol liquid water driven by anthropogenic inorganic salts: implying its key role in haze  
674 formation over the North China Plain, *Environ. Sci. Tech. Lett.*, 5, 160-166,  
675 <https://doi.org/10.1021/acs.estlett.8b00021>, 2018.

676 Zhang, F., Wang, Y., Peng, J., Chen, L., Sun, Y., Duan, L., Ge, X., Li, Y., Zhao, J., Liu, C., Zhang, X.,  
677 Zhang, G., Pan, Y., Wang, Y., Zhang, A. L., Ji, Y., Wang, G., Hu, M., Molina, M. J., and Zhang, R.:  
678 An unexpected catalyst dominates formation and radiative forcing of regional haze, *Proc. Natl. Acad.*  
679 *Sci. U.S.A.*, 117, 3960, <https://doi.org/10.1073/pnas.1919343117>, 2020.

680 Yu, C., Liu, D., Broda, K., Joshi, R., Olfert, J., Sun, Y., Fu, P., Coe, H., and Allan, J. D.: Characterising  
681 mass-resolved mixing state of black carbon in Beijing using a morphology-independent measurement  
682 method, *Atmos. Chem. Phys.*, 20, 3645-3661, <https://doi.org/10.5194/acp-20-3645-2020>, 2020.

683 Zhang, S. L., Ma, N., Kecorius, S., Wang, P. C., Hu, M., Wang, Z. B., Größ, J., Wu, Z. J., and  
684 Wiedensohler, A.: Mixing state of atmospheric particles over the North China Plain, *Atmos. Environ.*,  
685 125, Part A, 152-164, <https://doi.org/10.1016/j.atmosenv.2015.10.053>, 2016.

686 Zhang, Y., Zhang, Q., Cheng, Y., Su, H., Kecorius, S., Wang, Z., Wu, Z., Hu, M., Zhu, T., Wiedensohler,  
687 A., and He, K.: Measuring the morphology and density of internally mixed black carbon with SP2  
688 and VTDMA: new insight into the absorption enhancement of black carbon in the atmosphere, *Atmos.*  
689 *Meas. Tech.*, 9, 1833-1843, <https://doi.org/10.5194/amt-9-1833-2016>, 2016.

690 Zhang, Y., Du, W., Wang, Y., Wang, Q., Wang, H., Zheng, H., Zhang, F., Shi, H., Bian, Y., Han, Y., Fu,  
691 P., Canonaco, F., Prévôt, A. S. H., Zhu, T., Wang, P., Li, Z., and Sun, Y.: Aerosol chemistry and  
692 particle growth events at an urban downwind site in North China Plain, *Atmos. Chem. Phys.*, 18,  
693 14,637-14,651, <https://doi.org/10.5194/acp-18-14637-2018>, 2018.

694 Zhang, Y., Liu, H., Lei, S., Xu, W., Tian, Y., Yao, W., Liu, X., Liao, Q., Li, J., Chen, C., Sun, Y., Fu, P.,  
695 Xin, J., Cao, J., Pan, X., and Wang, Z.: Mixing state of refractory black carbon in fog and haze at  
696 rural sites in winter on the North China Plain, *Atmos. Chem. Phys.*, 21, 17631-17648,  
697 <https://doi.org/10.5194/acp-21-17631-2021>, 2021.

698 Zhou, C., Zhang, H., Zhao, S., and Li, J.: Simulated effects of internal mixing of anthropogenic aerosols  
699 on the aerosol-radiation interaction and global temperature, *Int. J. Climatol.*, 37, 972-986, 2017.

700